Miniaturization and Optimization of a DC–DC Boost Converter for Photovoltaic Application by Designing an Integrated Dual-Layer Inductor Model

Mohammed Ridha Benzidane, Rabia Melati, Mansour Benyamina, Said Meskine, Pierre Spitéri, Abdelkader Boukortt, Tekkouk Adda Benattia

Miniaturization and optimization of a DC-DC boost converter for photovoltaic application by designing an integrated dual-layer inductor model

Mohammed Ridha BENZIDANE[1*], Rabia MELATI[1,2], Mansour BENYAMINA[1], Said MESKINE[1], Pierre SPITERI[3], Abdelkader BOUKORTT[1], Tekkouk ADDA BENATTIA[1]

[1]Laboratoire d'Elaboration Caractérisation Physico Mécanique et Métallurgique des Matériaux (ECP3M), Electrical Engineering Department, Abdelhamid Ibn Badis University, Route natoinale N 11, kharouba, 27000 Mostaganem Algeria.

[2]Laboratory of Applied Power Electronic (LEPA), University of Sciences and Technology of Oran (USTO-MB), 31000, Algeria.

[3]INP-ENSEEIHT, IRIT, Toulouse, France

Corresponding author name; Mohammed Ridha BENZIDANE
E-mail: ridha.benzidane.etu@univ-mosta.dz

ACKNOWLEDGMENT

The authors would like to express their sincere thanks to (DGRSDT) the Algerian General Directorate of Scientific Research and Technological Development.

Miniaturization and optimization of a DC-DC boost converter for photovoltaic application by designing an integrated dual-layer inductor model

Abstract

For the sake of reducing the size of the power converters for photovoltaic applications, the microelectronics industry knows a permanent race in order to reach out to integrated electronic components with high efficacy and low losses for different applications. This paper presents a detailed study for designing an integrated structure with a dual-layer inductor model associated with two layers of MPP Molypermaloy magnetic cores. This inductor is intended to a DC-DC boost converter for photovoltaic application purposes. With an input of 17V, 220V output and supports a maximum current of 7A on an operating frequency of 500kHz with an output ripple less than 0.8%. The research covered the impact of coil's conductor thickness on the inductance. The gap effect study reached to determine the optimum gap between coils permit for the better profiteering of the mutual inductance with low losses. The transmission lines method was used to determine the equivalent electrical circuit for the designed dual-layer inductor to investigate the losses due to the parasite-flowing currents, also, to validate the performance and the well operating of the inductor in the application. The study investigated the magnetic behaviour and current density in conductors by numerical simulation governed by Maxwell's equations and solved by finite element method. An algorithm has been associated with the converter to compensate all losses and ensure the stability of the output voltage. The designed inductor has an inductance of 14.2µH and covering a volume of $10mm \times 10mm \times 2.07mm$.

1. Introduction

Nowadays, renewable energy technologies can compete with traditional energy sources. However, the current power conversion systems often suffer from a lack of optimization, which makes them still too expensive, with significant gaps in performance and reliability. Although many research proves the viability of sources such as photovoltaic (PV) or wind energy [1], there are also many reluctances to install these systems on a large scale. Besides, several technical problems must be solved to bring these systems to a sufficient degree of maturity to make them industrial products in their own right.

The problems concern as much the photovoltaic conversion material, which remains expensive to synthesize, as the electrical conversion chain, which has many losses during poorly adapted uses. Many specific control laws to optimize the production of photovoltaic energy also have some failures.

For the moment, studies conducted on the optimization of static energy converters can be generalized to several applications concerning their power supplies. The objectives are to minimize the size and the volume while limiting the development costs of the new products and reducing in particular the phases of real prototyping [4], regardless of the type of targe applications (photovoltaic, aerospace, telecommunications). The new power converters must be semi-integrated or, in the near future, fully integrated.

In short, the goal, in future years, is to achieve high conversion efficiencies with new power supplies having very small sizes. However, many problems must be solved, such as the optimization of integrated active elements [5, 8], the integration of passive components, the increase of working frequencies, in general, the knowledge of the interactions of the different functions constituting a power supply. The major problem which opposed today to the integration, the modularity and the standardization of the static converters, it's indeed the passive components, in particular the coils.

2. Electrical parameters of the converter

The contribution of our research is to concept a suitable method to reduce the size of a DC-DC boost converter in order to integrate it at the back of the photovoltaic module. The chosen application topology is the parallel modular chopper topology. The chopper acts as the interface between the output of the PV module and the DC bus. The concept to be created must conform to the crystalline photovoltaic module of the current market. The chopper must be able to handle an input voltage of 0 to 17 volts. 7 A is the maximum input current that must be supported. The rated output voltage is 220V. Overall, the system comprises a PV generator and an MPPT system which sends to the chopper a square wave with a duty cycle D adjusted according to the voltage delivered by the PV generation. The duty cycle varies depending on the input provided by the PV panel. This variability allows the output voltage to remain stable. The electrical diagram for the selected DC-DC boost converter is depicted in Figure 1.

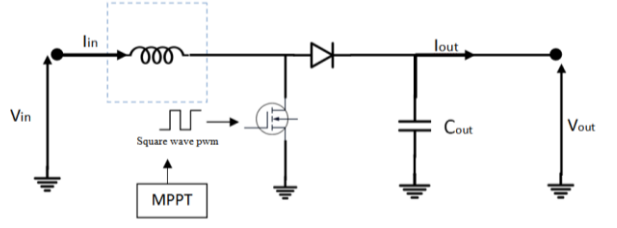

Figure 1: Electrical schematic for DC-DC boost converter.

The converter parameters are computed according to the specifications presented in table 1:

Operating frequency f	500 kHz
Input voltage V_{in}	17 V
Output voltage V_{out}	220V
Maximum current of the coil I_{Lmax}	7A
The average coil current I_{Lavg}	5A
Operating temperature T	Till 80°C
Ripple of the output ΔV_{out}	<0.8%

Table 1: Main specifications of the converter.

The duty cycle D value is around 92.27% calculated from the equation 1. it's possible to deduct from the previous equations that the output voltage is related directly to the duty cycle *D*. That implies that adjusting the duty cycle D value to correct the output is always possible since the solar panels create varying output throughout the day based on various factors. [9]. To determinate the Value of inductance L. need firstly to calculate the coil current ripple ΔI_L from equation 2

$$D = 1 - \frac{V_{in}}{V_{out}} \quad (1)$$

$$I_{L\max} = I_{Lavg} + \frac{\Delta I_L}{2} \quad (2)$$

$$L = \frac{V_{in} \times D}{f \times \Delta I_L} \quad (3)$$

The inductance value obtained from equation 3 is 7.82 µH. to reduce the maximum current I_{Lmax} flowing in the inductor, the inductance is increased to 10 µH. The capacitor C_{out} value of 40.674×10^{-8}F is calculated from equation 4. I_{out} is the output current calculated from equation 5. ΔV_{out} is the output voltage ripple that is equal to 0.8% of output voltage (1.76 V) as it's mentioned in table 1.

$$C_{out} = \frac{I_{out} \times D}{f \times \Delta V_{out}} \quad (4)$$

$$I_{out} = \frac{I_{in} \times V_{in}}{V_{out}} \quad (5)$$

3. Geometric dimensioning of the coil and its magnetic core

The coil that we want to integrate in the boost converter is of the square planar spiral type. Its geometrical dimensioning is carried out in two stages: the dimensioning of the magnetic core and the dimensioning of its winding

3.1. Single layer square spiral planar inductor

The dimensions reserved on the electronic converter board for our planar spiral inductor are: 12mm x 12mm x 10mm. The dimensions of its geometric parameters are given in Table 2, its geometry and its electrical circuit are presented in Figure 2. L is the inductance, Rs is the conductor's self-resistance calculated from equation 6. Cs represents the inter-turns coupling capacity calculated by equation 7. L_{moy} is the average internal and external length of the inductor, L_{active} is the length of the active area contribute in the creation of C_s

$$R_S = \rho \frac{l_{moy}}{w.t} \quad (6)$$

$$C_s = \varepsilon_0 . \frac{t.l_{active}}{s} \quad (7)$$

The conductor thickness value "t" strongly influences the values of the self-resistance Rs and the coupling capacitance Cs, which makes the inductance L very dependent on this thickness. The choice of the thickness "t" is therefore very critical and requires careful study.

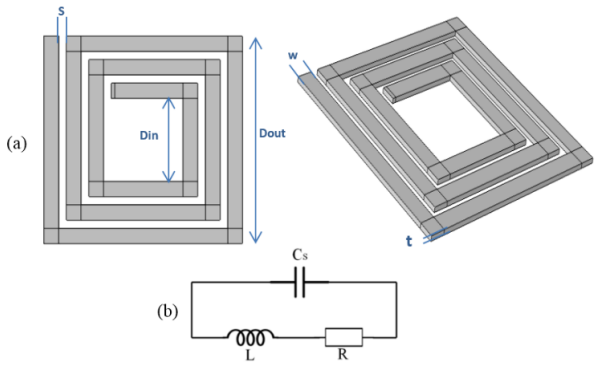

Figure 2: The square planar coil geometry proposed **(a)** 3D model for the propped coil's geometry **(b)** The electrical equivalent schematic.

Dout	Din	s	w
10 mm	4 mm	390 µm	470 µm

Table 2: Geometrical parameters.

3.2. The influence of the conductor thickness on the inductance value

A numerical simulation was done for the geometry presented in Figure 2(a). By varying the thickness value "t" from 5 µm to 600 µm we studied its influence on the inductance L. Simulation results are obtained by solving Maxwell's equations ($\nabla\vec{J} = 0,\ \nabla \times \vec{A} = \vec{B},\ \nabla \times \vec{H} = \vec{J},\ \overrightarrow{E} = -\nabla V,\ \overrightarrow{J} = \sigma\overrightarrow{E}$) that remain valid in all settings investigated. As a result, we will only discuss the physical models and boundary conditions that are unique to each situation.
According to the simulation findings, figure 3 depicts the influence of thickness on the inductance of a single layer inductor. Between these two factors, an inversely proportional relation was observed. Following the results analysis, equation 8 is formulated to characterise the inductance behaviour. Where L is the inductance, t is the thickness of the conductor, P1, P2, P3, P4 are the expression coefficients as presented on table 3. Expression 8 is plotted with the red line in figure 3, it fits 97% of the obtained results.

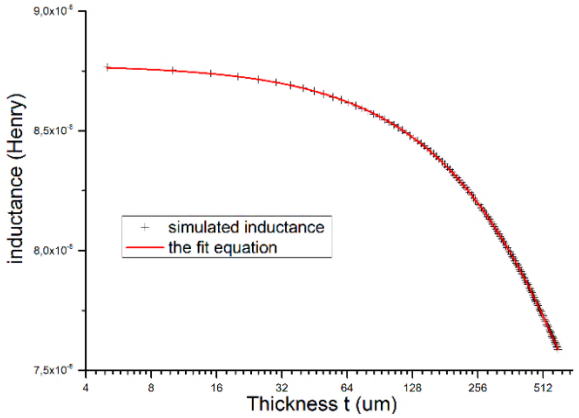

Figure 3: The effect of conductor thickness on the inductance.

$$L = \left(P_1 \times e^{\left(\frac{-t}{P_2}\right)} \right) + P_3 + \left(P_4^t\right) \qquad (8)$$

P_1	P_2	P_3	P_4
3,82249E-7	4758,70836	-2,94489E-7	5,56531E-11

Table 3: reached expression coefficients.

3.3. Selection of the optimal conductor thickness

The choose of the optimal thickness t allows to keep the size conductor within the permitted range without causing problems like overheating from skin effect or a lack of power from high losses. For it, a numerical simulation was done to observe the magnetic flux and current density for three samples of different thickness t: [60µm, 185µm, and 350µm]. The same initial condition applied to solve the problem by finite element method. The numerical results are presented on figure 4. It's noticeable a substantial increase in magnetic flux density for thin layers compared to thicker layers; this is related to the density of electric current in the conductor, which is more important in thin layers (figure 4(D)). The magnetic flux density kept the same form for all thicknesses, although the peaks had different values. These peaks correspond to the current density presented in figure 5.
The first proposal (60 µm) is excluded because of the high current density. Especially at the edges overlooking to the interior, which raises the risk of overheating. The third case is also excluded (350 µm). because we notice a skin effect well visible in figure 4 (D) and confirmed by figure 5, this will increase the resistance Rs and degrade the quality factor of the inductor The thickness t=185µm was chosen for its good current density associated to the low electromagnetic volumetric loss density (table 4). Much higher current densities are used in planar spiral inductors [21] [24], compared to the applicable density at 185m, implying that it is much safer and away of damage, especially given our ambitions to use this application in a challenging environment.

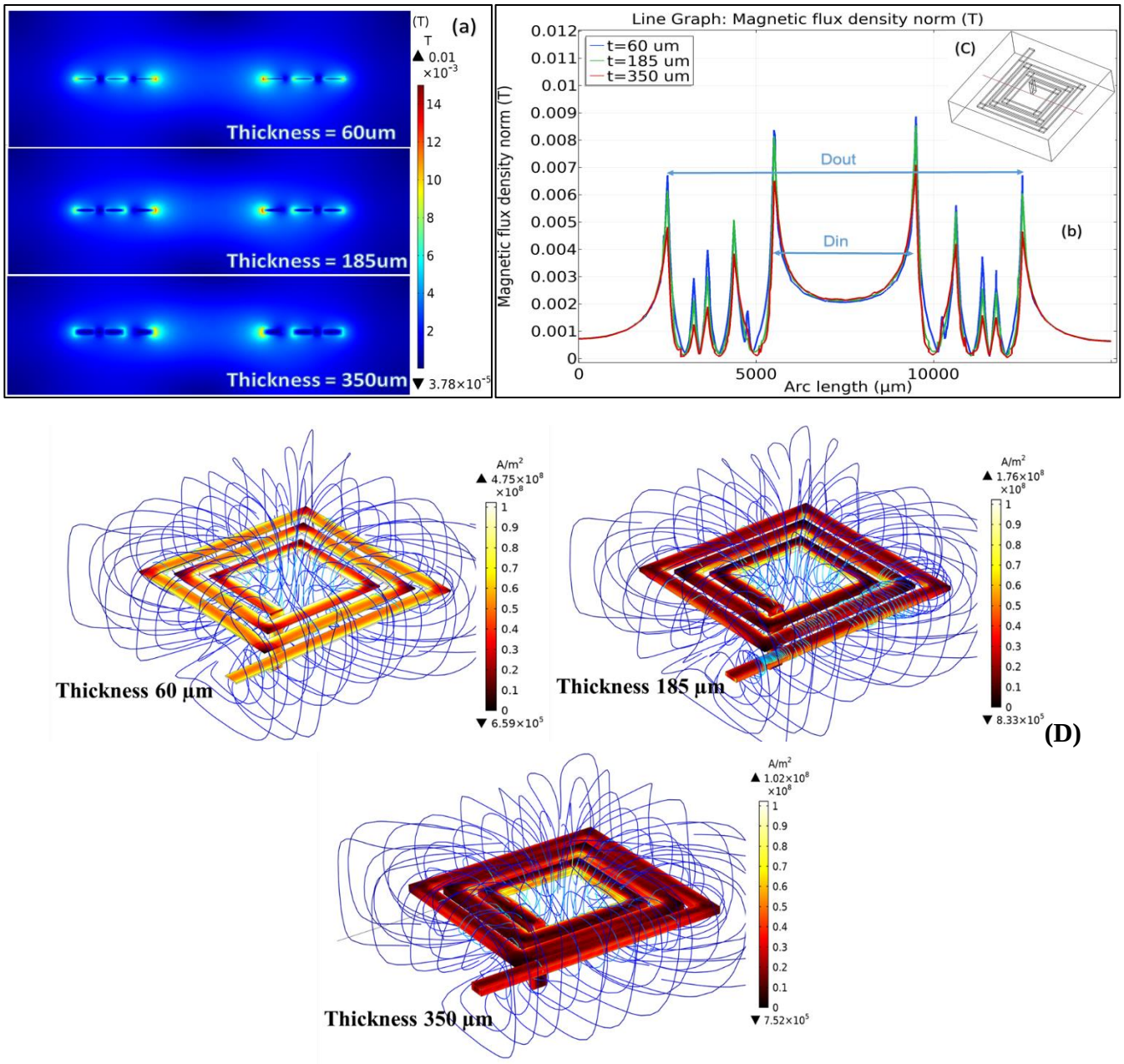

Figure 4: (a): 2D cross section shows the magnetic flux density (b:) Cross-sectional plot magnetic flux density along the arc length mentioned in (c). (D): 3D view for the current density and magnetic flux streamlines for each case.

Thickness t(μm)	Inductance (DC/500kHz)	Current density	Electromagnetic volumetric loss density (w/m^3)	
			DC	500kHz
60	$(7.02/6.89) \times 10^{-8} H$	$1.15 \times 10^{8} A/m^2$	$7.88 \times 10^{9} w/m^3$	$9.84 \times 10^{7} w/m^3$
185	$(6.76/6.45) \times 10^{-8} H$	$3.92 \times 10^{7} A/m^2$	$7.90 \times 10^{9} w/m^3$	$1.73 \times 10^{7} w/m^3$
350	$(6.45/5.82) \times 10^{-8} H$	$2.54 \times 10^{7} A/m^2$	$7.94 \times 10^{9} w/m^3$	$9.23 \times 10^{6} w/m^3$

Table 4: Comparison of measured Values for different thicknesses.

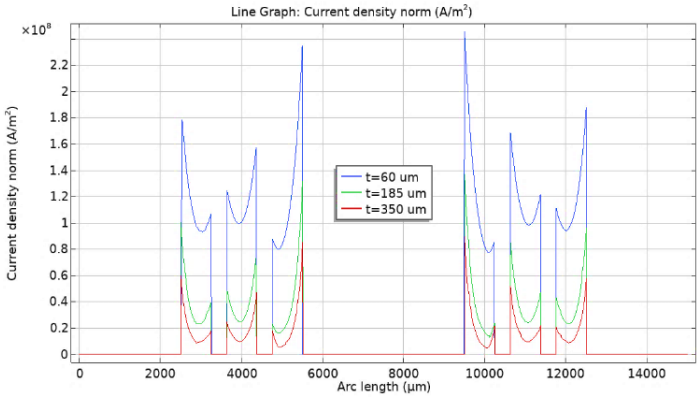

Figure 5: Simulations of the current density norm according to the arc length mentioned in figure 4 (c).

3.4. Dual-layer square planar spiral inductor

The measured inductance value (table 4) for the chosen thickness (180μm) is slightly lower than the calculated value, to increase it, we proceed as follows:

To increase the inductance value, our planar coil will be designed as two square planar spiral coils stacked one above the other (figure 6). Both coils are connected via a connecting bridge through the inner last turn. The coils were intentionally placed in this position to take advantage of the positive value of mutual inductance M (equation 9). Where L_T presents the global inductance of the dual-layer planar inductor shown in figure 9. L_1, L_2 are respectively, the self-inductance of coil 1 and coil 2. M is the mutual inductance generated between the coils. The direction of current passing through the coils determines the sign of mutual inductance. [25-27].

$$L_T = L_1 + L_2 \pm 2M \qquad (9)$$

Mutual inductance is mostly determined by the location and distance between the coils. Due to the interaction of the produced magnetic flux between both coils windings, which form a relatively significant electromagnetic field, the mutual inductance M assumes greater values for short distances. We have numerically simulated the electromagnetic field of the double-layer planar inductor for air gap lengths D varying in the range [60 μm; 1500 μm]. Results of simulation are depicted in Figure 7. It clearly appears that the increase of the gap, decreases the value of the overall inductance LT.

Expression 10 has been formulated and it describes the variation of the global inductance LT as a function of the gap D. a, b and c are the expression's coefficients presented in Table 5. They could be deferred for the same geometry with different parameters.

D represents the gap distance separated between inductors. The red line plots equation 10 in Figure 7, where it fits the simulated results with a precision of 98.7%.

$$L_T = a + b \times D^c \qquad (10)$$

a	b	c
2,23508E-7	-6,105E-10	0,64518

Table 5: Reached expression coefficients.

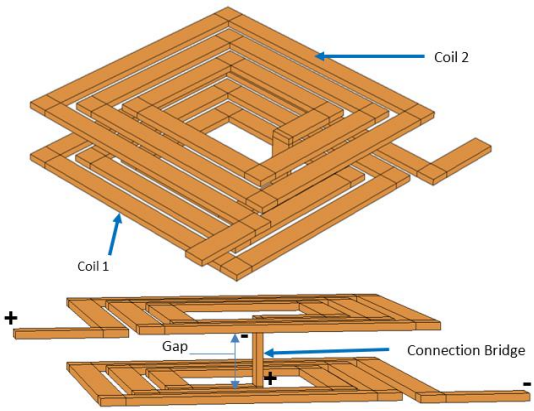

Figure 6: 3D presentation of double layer square spiral planar inductor without magnetic material (two different views angles).

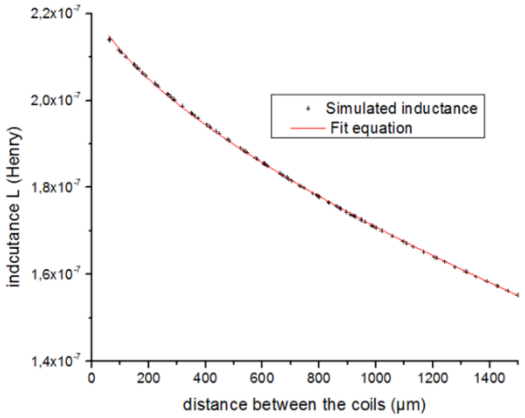

Figure 7: The effect of the gap on the overall inductance.

The capacitive effect created between coils layers must be well consider while choosing the gap. Because the coupling capacity C_{gap} between the coils significantly (Figure 10) impacts the inductor's role and yield

The value of this capacitor is related to the interaction area between both coils shown on figure 8. The C_{gap} coupling capacity strongly depends on the relative permittivity of the dielectric material, so the choice of material is very important. The Kapton-Polyimide is recommended because, it's extremely durable and provides a low dielectric loss over a wide frequency range and high breakdown voltage. Furthermore, an excellent balance of properties over a wide range of temperatures [28] [30]. Its relative permittivity is about 3.85.

In order to study the influence of the coupling capacity C_{gap} on the inductor, a comparison is done for two cases with and without Kapton by varying the gap (figure 9).

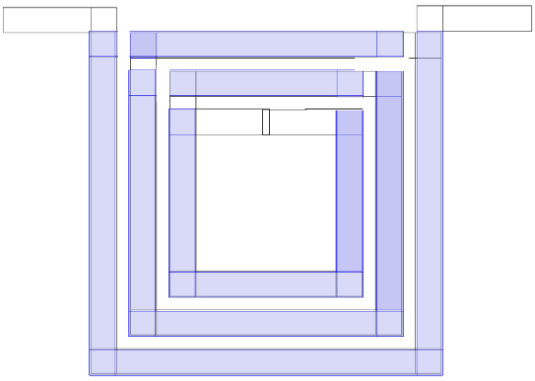

Figure 8: Top view of the interactive section between the two planar coils.

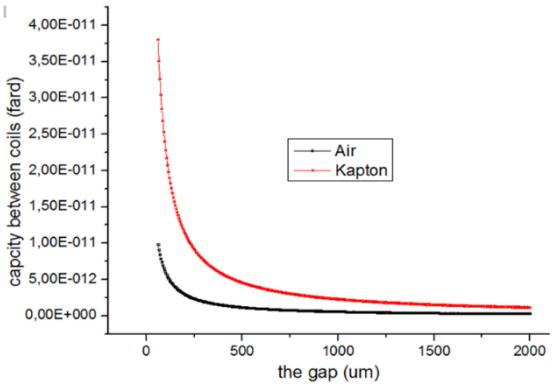

Figure 9: The curve showing the variation of capacity generated based on the gap (with/without Kapton).

Figure 9 shows the collected findings as a curve that could be split into two intervals. In the first, Cgap capacity takes more important values for small gaps, in particular, with the insertion of the dielectric. This leads to an increase in the leakage electrical current, hence, a lower efficiency of the inductor. We notice, also that the Cgap capacity varies sharply in

response to the variation of the gap D, selecting a gap in this range is entirely ruled out. In the second interval, the Cgap capacity takes smaller values and the variation of the gap D has less significant influence on the Cgap capacity.

Although the value of the Cgap capacity is slightly higher with the insertion of the Kapton, there is no technical way to avoid it, because it's taking the role of support and isolation between the inductors and avoids the dynamic instability of the dual-layer inductor.

The C_{gap} capacity generated for a gap of 500µm is around $4.56 \times 10^{-12} F$, it is almost 8.4 times less than generated by a gap of 60µm ($38 \times 10^{-12} F$).

Before opting for the optimal value of the gap, we will simulate using PSIM software, the leakage currents for a gap of 60 µm and 500 µm. To carry out this simulation, we replaced the circuit of the perfect coil of the converter by equivalent circuit of the dual-layer figure 10 and we took into consideration the value of the self and mutual inductance for each case.

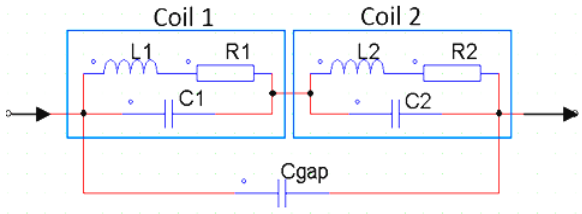

Figure 10: equivalent schematic for a dual-layer coil.

C1, C2 are respectively, the inter-turn parasitic capacitances of the first and second coils. R1, R2 are the respective ohmic resistances of their windings. C_{gap} is the capacity resulting from the capacitive effect generated between the two planar inductors.

Figure 11 represents the results of the simulating leaked current through the C_{gap}. The simulation displays an average value of $1.81 \times 10^{-3} A \; and \; 1.66 \times 10^{-2}$ for the respective gaps of 500 µm, 60 µm.

Based on the analysis of the obtained results, the optimal gap is 500µm because, it generates minimal losses. The corresponding inductance value is $1.9 \times 10^{-7} H$.

The distributions of the current densities in the dual-layer coil are simulated by the COMSOL Multiphysics software for the 60µm and 500µm gaps figure 12. This simulation shows that the current density in the space separating the two coils is greater for the 60µM gap. These results confirm our choice of the 500 µm gap.

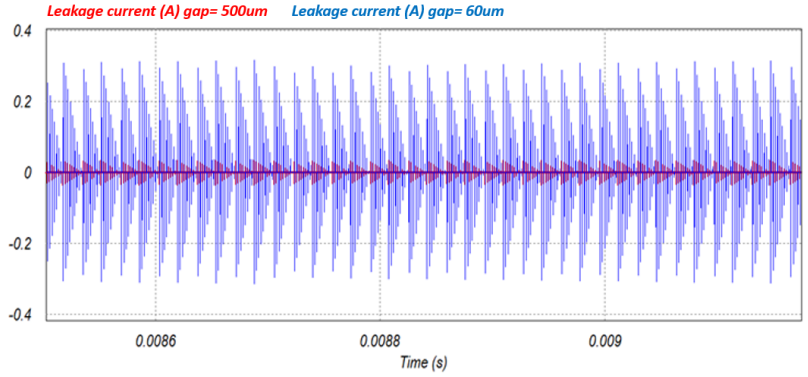

Figure 11: The simulated leaking current passed by the capacitor created between the layers for the different gaps.

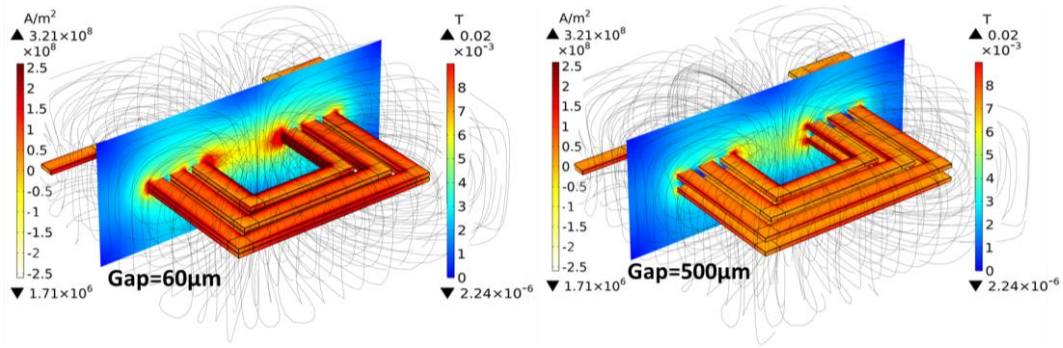

Figure 12: Current density, magnetic flux distribution in dual layer inductor for different gaps

4. Choice of the magnetic core

The role of the magnetic core in an inductor is mainly to increase the strength of the magnetic field as well as the value of the inductance. To increase the value of our dual-layer inductor from $1.9 \times 10^{-7} H$. which is the value measured for a gap of 500µm, up to the desired value 10µH, we have to choose the corresponding magnetic material. The selection of magnetic material is critical and accurate since it relies on several key characteristics: resistance, degradation relevant to the applied frequency, and magnetic permeability.

The ratio between the value of the desired inductance (10µH) and the measured value $(1.9 \times 10^{-7} H)$ is almost 53. As a result, the required permeability of the magnetic core must be at least 53. Following a literature review [34-37], we opted for Molypermalloy Powder (MPP). Molypermalloy Powder has a relative permeability of 60; it is mainly composed of 2% molybdenum, 81% nickel, and 17% iron. MPP offers high resistance, low hysteresis, negligible eddy current losses, and excellent inductance stability under DC and AC bias conditions. The saturation flux is approximately 8,000 Gauss (0.8 T).

The volume of the magnetic core is calculated according to the stored energy (equation 11) and the magnetic energy density of the material which is related to the maximum flux which the material can support (relation 12):

$$E = \frac{1}{2} L I_{\max}^{2} = 245 \mu J \qquad (11)$$

$$W_{v\max} = \frac{B_{\max}^{2}}{2\mu_0 \mu_r} = 4247\, J/m^{3} \qquad (12)$$

The volume of the magnetic core is given by relation 13:

$$V = \frac{E}{W_{V\max}} \approx 60 mm^{3} \qquad (13)$$

10% added to the volume to cover all the losses energy caused by applying frequency and the temperature, especially since this application is expected to be employed in a harsh environment, the magnetic core volume will divide into two equal flat layers [10mm X 10mm X0.4mm], where the final form showed in figure 13. A silicon layer is used as an inductor's substrate to raise the resistance to reduce parasite flow and for a good heat dissipation [38].

4.1. Modelling the resulting inductor

The design of the equivalent circuit of the inductors is an effective method to validate their good functioning.

The advantage of this method exemplifies the ability to provide anticipation for the behaviour description of the inductor placed on the electrical circuit and maximum optimization of parasitic effects [39-40]. The form diagram (figure 13) presents every path possible for flowing current and the physical nature modelling for this passing (resistance, capacitance, or inducing). We translate this diagram for an electrical equivalent model figure 14 in order to simulate the inductor behaviour.

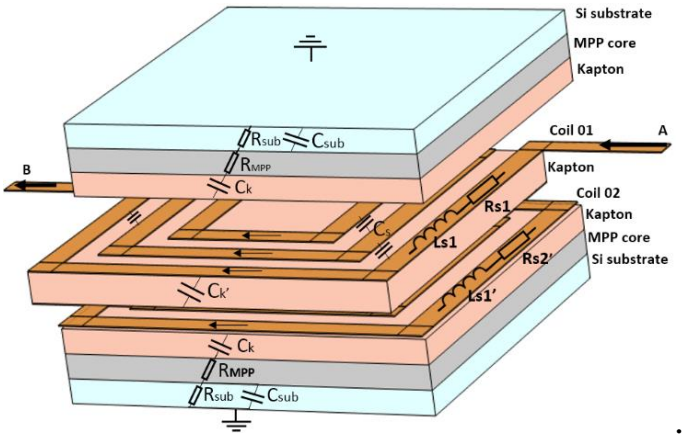

Figure 13: 3D Final structure of dual-layer planar spiral coil with parasitic elements illustration

The dual-layer inductor equivalent circuit contains two inductances Ls1, Ls2. The parasitic elements are: Rs1, Rs the series resistances which appears along the windings. C_{gap} the coupling capacity between the two coils. Ck: the parasitic capacitance between the conductive winding (conductor) and the magnetic core. R_{MPP} is the resistance associated with the magnetic layer, R_{sub} and Csub are respectively the resistance and the capacitance related to the silicon substrate. The analytical expressions of different elements constituting the electrical model are calculated via the following expressions:

$$R_{s1} = R_{s2} = \rho_{copper} \frac{l_{coil}}{t.w} \qquad (14)$$

$$R_{MPP} = 2.\rho_{MPP} \frac{t_{MPP}}{l.w} \qquad (15)$$

$$R_{sub} = 2.\rho_{si} \frac{t_{sub}}{l.w} \qquad (16)$$

$$C_{sub} = \frac{1}{2} \varepsilon_0 \varepsilon_{si} \frac{t_{sub}}{w.l} \qquad (17)$$

$$C_k = \frac{1}{2} \varepsilon_0 \varepsilon_{kapton} \frac{t_k}{w.l} \qquad (18)$$

Where:$\rho_{cu} = 1.7 \times 10^{-8} \Omega.m$,$\rho_{si} = 18.5 \Omega.m$, $\rho_{MPP} = 6 \times 10^{-7} \Omega.m$. $\varepsilon_{si} = 11.8$. $t_k = 150 \mu m$ $t_{sub} = 100 \mu m$ $l = 0.082 m$ The parameter **t** represents the thickness associated with each layer.
The parasitic elements present in figure 13, form the electrical circuit of the dual-layer inductor illustrated by figure 14.

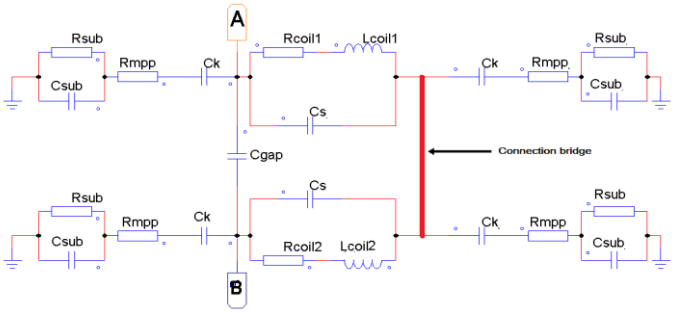

Figure 14: Equivalent electrical circuit of the dual-layer inductor

4.2. Simulations of currents and voltages wave curves

Figure 15 shows the boost DC/DC converter containing the equivalent electrical circuit of the dual-layer planar spiral coil. The output voltage, the current flowing in the inductor, and the output current are represented in Figure 16.

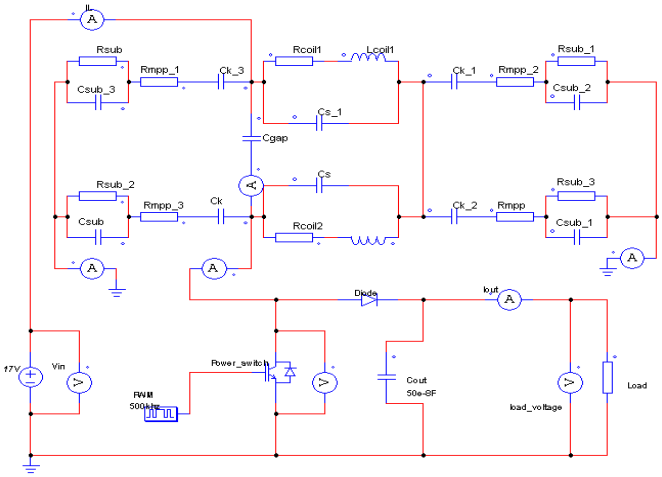

Figure 15: The DC/DC converter with the equivalent model of the dual-layer inductor

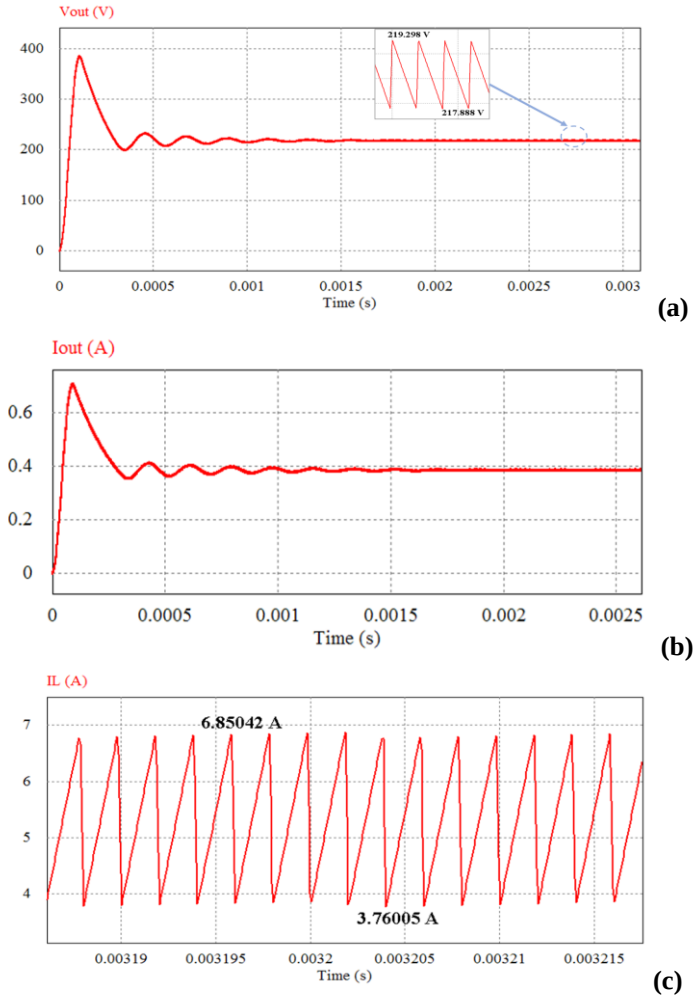

Figure 16/ Waveforms for the converter including the equivalent model, (a) Input and output waveform, (b) Output current (c) Current flowing in the inductor

The simulation results obtained show that the output current I_{out} and the output voltage V_{out} are continuous, conform to those of a DC / DC boost converter and their values are very close to those of the specifications. These results confirm that the coil is functioning correctly. We can therefore affirm that its geometrical dimensioning and its electrical circuit are well done.

We note, on the other hand, that the average value of the output voltage displays 218.61V, slightly lower than the desired voltage (220V) and a ripple not exceeding 0.8% (1.37V).

Collapse on the output voltage in a photovoltaic system is caused by changes in material properties due to several factors like temperature and humidity; shading is also one of the causes that favours this problem. In this work, we propose an adequate technique allowing to adjust the output voltage to 220V whatever the degradation of its input voltage received by the solar panel.

Obviously, the output voltage of a DC / DC boost is directly related to the duty cycle, so any change in the duty cycle results in the change in the output voltage. On this principle, we realized an algorithm whose flowchart is presented in figure 17 in order to sort the appropriate duty cycle to adjust the output voltage to 220V according to the received input voltage. The operation of this algorithm is based on direct supervision of the converter output. If the output voltage is lower or higher than the desired voltage (220V), the algorithm enters a loop which adjusts the duty cycle with a step of 0.01% until the desired voltage is reached and vice versa.

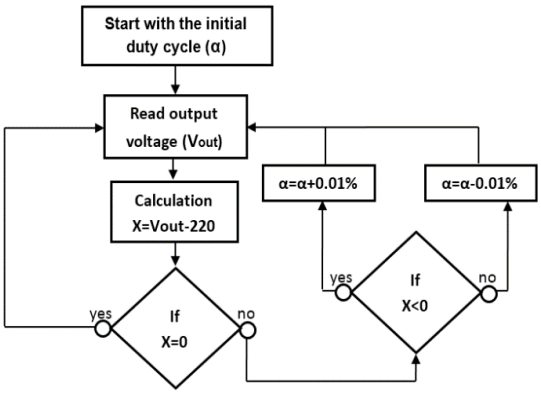

Figure 17 The organigramme form of duty cycle corrector.

The simulated waves of the output voltage, output current, and inductor current after the correction are shown in Figure 18. The findings demonstrate changing the output to the desired voltage due to algorithm. The provided results are substantially consistent with the set of circumstances.

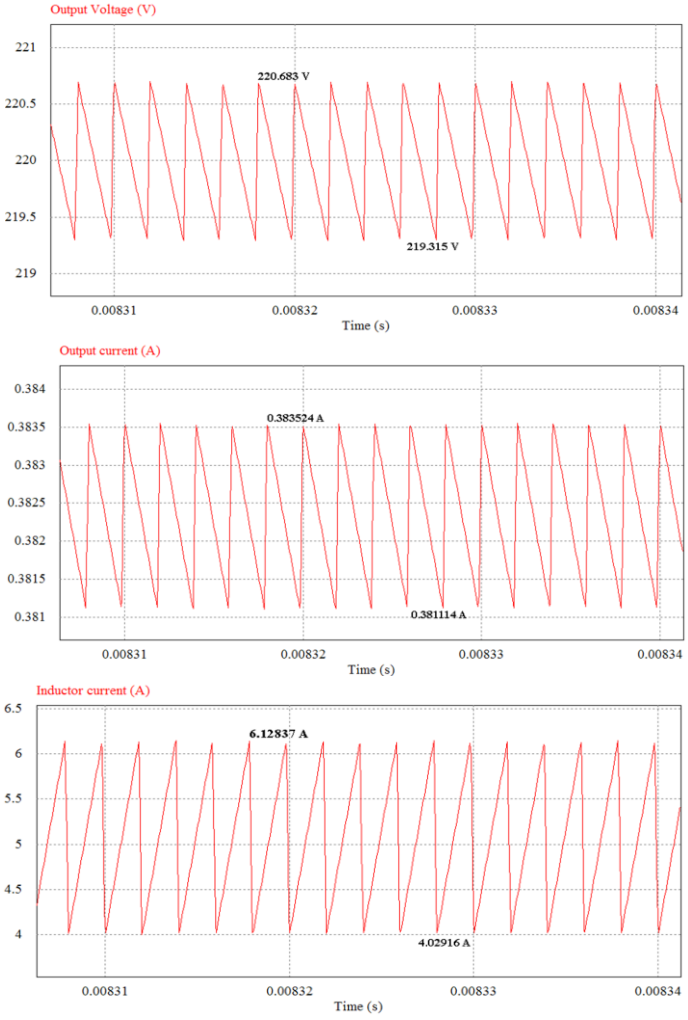

Figure 18: Presentation of simulated waves for; the Output voltage Vout, output current Iout, and the inductor current IL after correcting the duty cycle.

The results in Figure 18 show that the average output voltage increased from 218,61 to 219.997 with a ripple of 0.621% V_{out}, thanks to the algorithm. The duty cycle changed from 92.27% to 92.33%. We note that this technique gives good results and allows the converter to correct itself.

5. Electromagnetic simulation of the inductor

To make sure that our dimensioned dual-layer inductor can operate at long-term, without any heating problems and without

disturbing the neighbouring components, we simulated the distribution of its current density, as well as the distribution of the lines magnetic field and magnetic flux. The simulation done by COMSOL Multiphysics is based on the finite element method. Results are obtained by solving the Maxwell equations [41].
The inductance could be calculated from the total magnetic energy created by the current flowing through the coil using the formula 11. After solving the electromagnetic problem, the simulation shows an inductance value of 14.2µH at the converter's operational frequency (500KHz). This result is quite encouraging to validate our dimensioning.

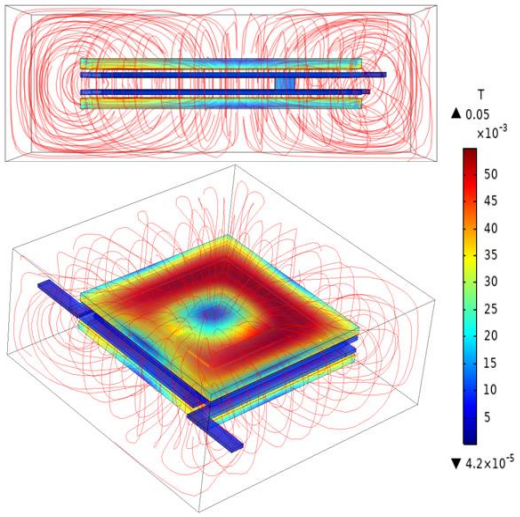

Figure 19 Magnetic field streamlines & Magnetic flux density in the dual-layer inductor

Figure 19 shows a good distribution of the magnetic field lines. The field lines envelop the two coils, which promotes good mutual inductance. We also notice that the magnetic field lines occupy a very small space around the dual-layer coil, so it cannot disturb neighbouring components. The value of the overall inductance measured by COMSOL software is 14. 2µH. Figures 19-20 show also a proper distribution of the magnetic flux density at the dual-layer inductor's core, which indicates excellent exploitation of the magnetic core. The active area records a magnetic flux value that does not exceed 0.055 T; this value is far from causing magnetic saturation of the core, because it is very low compared to the saturation induction of MPP (0.8T)

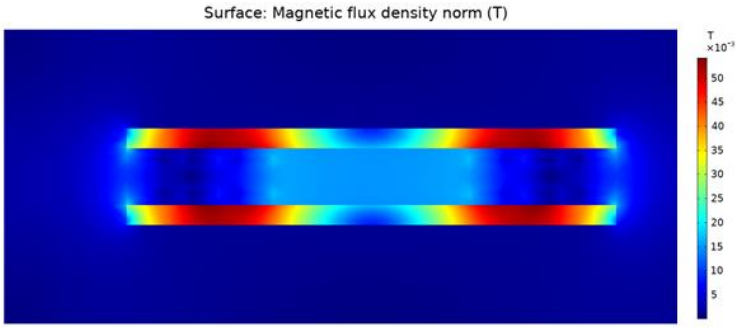

Figure 20: A cross-section of the inductor showing the magnetic flux density distribution

Figure 21 is a cross-section for the dual-layer inductor appears the distribution of the current density in coil's conductor**.**
The results show the absence of the skin effect phenomena, that's implies a significant attenuation of the losses by joules effect as well as the reduction of the series resistances Rcoil1 and Rcoil2. The lowest current density recorded on the conductor is around $9.85 \times 10^5 A/m$ that's implies the complete usage of the conductor. Moreover, there is no visible trace of direct or inverse proximity effect created between the top and bottom coil, indicating the flow of electrical current in the gap.
We notice more important current density in a small area in conductors adjacent to the inside diameter. It's caused mainly by the accumulation of magnetic field lines at the centre of the dual-layer inductor. The intensity did not exceed the limit that might pose a danger.

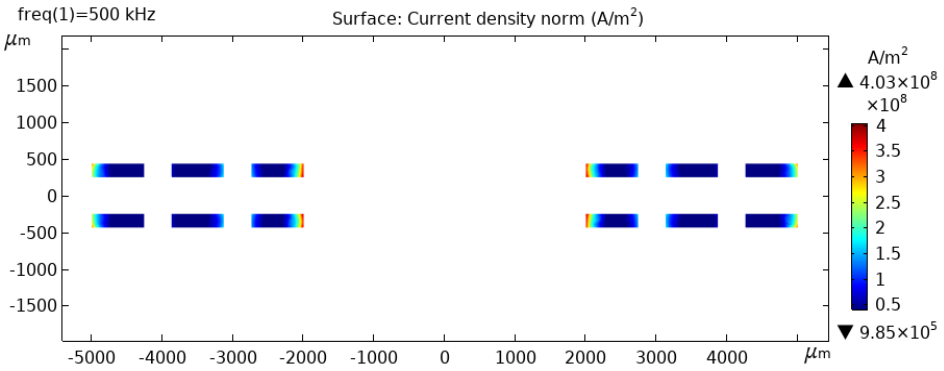

Figure 21 A cross-section for the inductor showing the current density distribution in the conductor

6. Conclusion

The work presented in this article is part of a research project working on the miniaturization of converters for photovoltaic systems, with the aim of their modularization and their standardization while maintaining their functionality and reliability at a low cost. The miniaturization of a DC / DC converter necessarily involves the miniaturization of its passive components which raises different problems to be solved. In this article we have worked on the miniaturization of the coil and the stability of the boost converter dedicated for photovoltaic energy. We chose a dual-layer square planar spiral coil that we dimensioned by taking into account the defects of this type of coils in order to correct them.

Staged inductors have the advantage of a very small volume, and of an inductance increased by the mutual inductance, but their major disadvantage is dynamic instability. Our coil has to support a current of 7A, which makes the study and correction of this defect essential. To solve this instability problem, we inserted a Kapton dielectric between the two staked coils.

To reduce the capacitive effect between the two coils, we studied the influence of the gap on the value of the parasitic capacitance resulting from this effect. This study was followed by the simulation of the parasitic currents flowing in the gap between the two coils as well as the simulation of their current density. This allowed us to choose the optimal thickness of the gap.

This work also included the study of the effect of the conductor thickness on the inductance. Following this study, we formulated an equation which makes it possible to calculate the value of the inductance according to the conductor thickness. After correcting all defects of the double stage coil, we validated its good functioning.

Various defects affect the solar panels and degrade the voltage delivered to the DC / DC converter. To solve this problem and stabilize the output voltage by maintaining it at the desired voltage (220V), we proposed a simple and reliable technique that gave good results.

References

[1] Abdou Tankari, Mahamadou. Système multi-sources de production d'énergie électrique: méthode de dimensionnement d'un système hybride et mise en œuvre expérimentale de l'optimisation de la gestion d'énergie. Diss. Le Havre, 2010.

[2] Nguyen, Nhat M., and Robert G. Meyer. "Si IC-compatible inductors and LC passive filters." IEEE Journal of Solid-state circuits 25.4 (1990): 1028-1031.

[3] Coulibaly, S., G. Loum, and K. A. Diby. "Design of Integrated LC Filter using Multilayer Flexible Ferrite Sheets." IOSR Journal of Electrical and Electronics Engineering (IOSR-JEEE) 10.6 (2015): 35-43.

[4] Koh, Kisik, et al. "Core-shell magnetic nanoparticles for on-chip RF inductors." 2013 IEEE 26th International Conference on Micro Electro Mechanical Systems (MEMS). IEEE, 2013.

[5] Mishra, Dibyajat, P. Markondeya Raj, and Rao Tummala. "Design, fabrication and characterization of thin power inductors with multilayered ferromagnetic-polymer composite structures." Microelectronic Engineering 160 (2016): 34-38.

[6] Meyer, Christopher D., et al. "A micromachined wiring board with integrated microinductor for chip-scale power conversion." IEEE Transactions on Power Electronics 29.11 (2014): 6052-6063.

[7] Vighetti, Stéphane. Systèmes photovoltaïques raccordés au réseau: Choix et dimensionnement des étages de conversion. Diss. Institut National Polytechnique de Grenoble-INPG, 2010.

[8] Sabiri, Zakaria, et al. "DC/DC converters for photovoltaic applications-modeling and simulations." 2014 International Renewable and Sustainable Energy Conference (IRSEC). IEEE, 2014.

[9] Sarwar, Jawad, et al. "Description and characterization of an adjustable flux solar simulator for solar thermal, thermochemical and photovoltaic applications." Solar Energy 100 (2014): 179-194.

[10] He, Liangzong. "A novel quasi-resonant bridge modular switched-capacitor converter with enhanced efficiency and reduced output voltage ripple." IEEE Transactions on Power Electronics 29.4 (2013): 1881-1893.

[11] Mohan, Sunderarajan S., et al. "Simple accurate expressions for planar spiral inductances." IEEE Journal of solid-state circuits 34.10 (1999): 1419-1424.

[12] Bryan, H. E. "Printed inductors and capacitors." Tele-Tech & Electronic Industries 14.12 (1955): 68.

[13] Kouril, Lukas, et al. "Coil optimization with aid of flat coil optimizer." Proceedings of the 5th WSEAS congress on Applied Computing conference, and Proceedings of the 1st international conference on Biologically Inspired Computation. World Scientific and Engineering Academy and Society (WSEAS). 2012.
[14] Terman, F. E. "Section 2: Circuit Elements." Radio Engineers' Handbook, First Edition, New York, NY: McGraw-Hill Book Company (1943).
[15] Zhang, Wei, et al. "Design for efficiency optimization and voltage controllability of series–series compensated inductive power transfer systems." IEEE Transactions on Power Electronics 29.1 (2013): 191-200.
[16] Wheeler, Harold A. "Simple inductance formulas for radio coils." Proceedings of the institute of Radio Engineers 16.10 (1928): 1398-1400.
[17] Ruehli, Albert, Giulio Antonini, and Lijun Jiang. "Skin Effect Modeling." (2017): 213-248.
[18] Biro, Oszkar, et al. "Voltage-driven coils in finite-element formulations using a current vector and a magnetic scalar potential." IEEE transactions on magnetics 40.2 (2004): 1286-1289.
[19] Rotella, Francis M., Volker Blaschke, and David Howard. "A broad-band scalable lumped-element inductor model using analytic expressions to incorporate skin effect, substrate loss, and proximity effect." Digest. International Electron Devices Meeting. IEEE, 2002.
[20] Sullivan, Charles R. "Computationally efficient winding loss calculation with multiple windings, arbitrary waveforms, and two-dimensional or three-dimensional field geometry." IEEE transactions on power electronics 16.1 (2001): 142-150.
[21] Chen, Mingming, et al. "Characteristics of double planar micro-inductor with patterned NiFe thin-films for DC/DC integration." Micromachines 8.5 (2017): 151.
[22] Vanukuru, Venkata Narayana Rao, and Anjan Chakravorty. "High density solenoidal series pair symmetric inductors and transformers." IEEE Transactions on Electron Devices 61.7 (2014): 2503-2508.
[23] Medjaoui, Fatima Zohra, et al. "Conception and manufacturing of a planar inductance on NiFe substrate." Transactions on Electrical and Electronic Materials 20.3 (2019): 269-279.
[24] Ahmed, Mohamed H., et al. "High-efficiency, high-density isolated/regulated 48V bus converter with a novel planar magnetic structure." 2019 IEEE Applied Power Electronics Conference and Exposition (APEC). IEEE, 2019.
[25] Babic, Slobodan, and Cevdet Akyel. "New formulas for mutual inductance and axial magnetic force between magnetically coupled coils: thick circular coil of the rectangular cross-section-thin disk coil (pancake)." IEEE Transactions on Magnetics 49.2 (2012): 860-868.
[26] Joy, Ezhil Reena, Ankit Dalal, and Praveen Kumar. "Accurate computation of mutual inductance of two air core square coils with lateral and angular misalignments in a flat planar surface." IEEE transactions on magnetics 50.1 (2013): 1-9.
[27] Liu, Tao, et al. "Inductance calculation of multilayer circular printed spiral coils." Journal of Physics: Conference Series. Vol. 1176. No. 6. IOP Publishing, 2019.
[28] Mittal, Kash L. Polyimides and Other High Temperature Polymers: Synthesis, Characterization and Applications, volume 2. CRC Press, 2003.
[29] DuPon Kapton HN Polyimide Film; datasheet 2019 available online: https://www.dupont.com/electronic-materials/polyimide-films.html/
[30] Virtanen, Juha, et al. "Inkjet-printed humidity sensor for passive UHF RFID systems." IEEE Transactions on Instrumentation and Measurement 60.8 (2011): 2768-2777.
[31] Magambo, Jean Sylvio Ngoua Teu, et al. "Planar magnetic components in more electric aircraft: Review of technology and key parameters for DC–DC power electronic converter." IEEE Transactions on Transportation Electrification 3.4 (2017): 831-842.
[32] Rao, Bo, et al. "Reduction of leakage inductance and AC resistance of planar transformers by optimising the current distribution." IET Power Electronics 11.3 (2018): 501-506.
[33] Ouyang, Ziwei, and Michael AE Andersen. "Overview of planar magnetic technology—Fundamental properties." IEEE Transactions on Power Electronics 29.9 (2013): 4888-4900.
[34] Silveyra, Josefina M., et al. "Soft magnetic materials for a sustainable and electrified world." Science 362.6413 (2018).
[35] Ray, Biswajit, et al. "Low temperature performance of a boost converter with MPP and HTS inductors." Proceedings of Applied Power Electronics Conference. APEC'96. Vol. 2. IEEE, 1996.
[36] SWIHART, Mark A. Inductor cores–material and shape choices. Magnetics®-www. mag-inc. com, 2004.
[37] Ouyang, Gaoyuan, et al. "Review of Fe-6.5 wt% Si high silicon steel—A promising soft magnetic material for sub-kHz application." Journal of Magnetism and Magnetic Materials 481 (2019): 234-250.
[38] Tsuji, Kenichi, et al. "Heat conductive silicone composition based on combination of components, heat conductive layer, and semiconductor device." U.S. Patent No. 9,698,077. 4 Jul. 2017.
[39] Melati, Rabia, et al. "Design of a new electrical model of a ferromagnetic planar inductor for its integration in a micro-converter." Mathematical and Computer Modelling 57.1-2 (2013): 200-227.
[40] Derkaoui, M., et al. "Design and modeling of an integrated micro-transformer in a flyback converter." Telkomnika 11.4 (2013): 669.
[41] Butler, Sam L., and Z. Zhang. "Forward modeling of geophysical electromagnetic methods using Comsol." Computers & Geosciences 87 (2016): 1-10.